Satellite Observations of Surface Deformation at the Coso Geothermal Field, California

Mariana Eneva[1], Andrew Barbour[2], David Adams[3], Vicky Hsiao[4a], Kelly Blake[5], Giacomo Falorni[4a] and Roberto Locatelli[4b]

[1]Imageair Inc., [2]USGS – Menlo Park, CA, [3]Independent Consultant, [4a]TRE Altamira Inc. - Canada, [4b]TRE Altamira s.l.r. - Italy, [5]U.S. Navy Geothermal Program Office

Keywords

Coso Geothermal Field, surface deformation, subsidence, InSAR, permanent scatterers, SqueeSAR, poroelastic deformation modeling, earthquakes

ABSTRACT

Surface deformation time series and rates are identified at the Coso Geothermal Field (CGF) and surrounding areas by applying interferometric synthetic aperture radar (InSAR) to satellite scenes from Envisat (June 2004 − October 2010) and Sentinel (November 2014 – April 2018). The measurements are done in the line of sight (LOS) to each satellite, within an area of size ~450 km^2, at the locations of hundreds of thousands permanent and distributed scatterers. Thirty descending (satellite moves north to south) and 45 ascending (south to north) images were used from Envisat, and 63 descending and 65 ascending from Sentinel. A decomposition into average vertical and east horizontal components is also performed in more than 35,000 100-m pixels where both types of LOS measurements are available. The main observations at CGF include: (1) a subsidence area of size ~70 km^2, with a maximum subsidence of –27.6 mm/year for the Envisat period and lower maximum subsidence of –19.1 mm/year for the Sentinel period; (2) eastward movements in the western part of the subsidence area, with Envisat maximum of +23.9 mm/year and a lower Sentinel maximum of +15.9 mm/year; (3) westward displacements in the eastern part of the subsidence area, with Envisat maximum of − 14.2 mm/year and Sentinel maximum of –11.9 mm/year; (4) very good agreement of the InSAR observations with leveling survey data; (5) earthquake clusters in the subsidence area and hypocentral cross-sections showing clusters at various depths and migration in time; and (6) good predictions of the overall geothermal resource, based on poroelastic modeling using both leveling and InSAR data. The ultimate goal of the project is to provide geothermal operators with tools that can be used in reservoir management.

1. Introduction

The Coso Geothermal Field (CGF) is located on the lands of the military-owned Naval Air Weapons Station at China Lake, in the central part of eastern California (Figures 1 and 2). It is
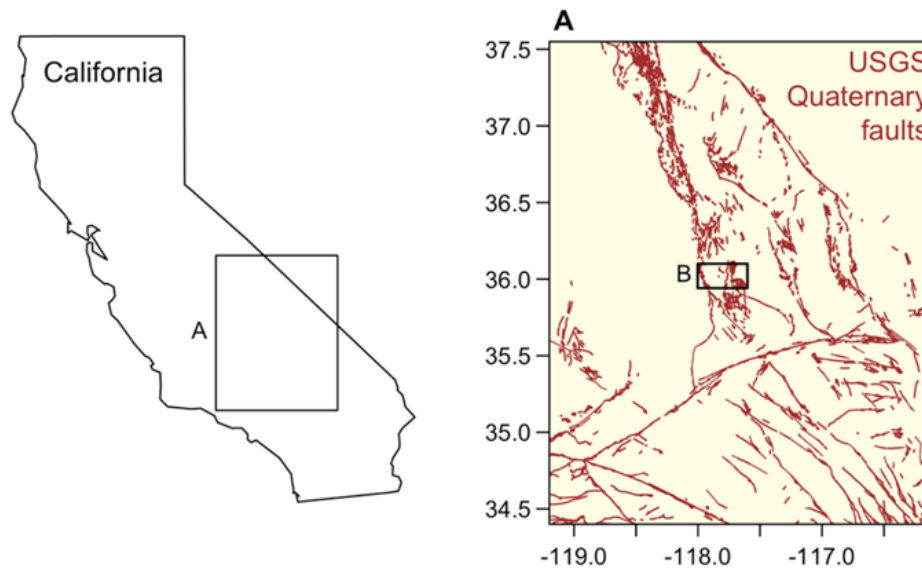
Figure 1. Location of study area and map showing fault lines. InSAR processing was carried out for area B.

managed by the U.S. Navy Geothermal Program Office (GPO), and is operated by the Coso Operating Company. It has been producing geothermal power since 1987 and currently has four operating plants, with a total of 270 MWe rated capacity (Monastero, 2002). The mean capacity of the Coso KGRA (Known Geothermal Resource Area – see Fig. 2) is estimated at 518 MWe (USGS, 2008).

The CGF is a volcanic field located in the area of a releasing bend step-over in a dextral strike-slip fault system. The shallow (<2 km) and very hot (200° - 328°C) resource is related to local crustal thinning (Monastero, 2002). There are numerous surface manifestations of geothermal activity, including fumaroles, hot springs, hydrothermally altered rocks, and Late Cenozoic volcanics including 37 rhyolite domes. At least three sets of faults are mapped in the region, controlling most of the volcanic and geothermal activity. There have been numerous geophysical studies at Coso, such as microseismicity studies and seismic velocity models (e.g., Seher, et al., 2011; Kaven, et al., 2011, 2012, 2014), a magnetotelluric experiment resulting in a 3D-resistivity model (Newman, et al., 2008), collection and analysis of gravity data (Monastero, et al., 2005), etc. Since the field is liquid-limited, injecting supplemental water into the reservoir to stabilize and enhance the field was implemented in December 2009, with the hope to increase electricity production by about 50 MWe. Water is pumped through a 14-km pipeline from two wells of the Hay Ranch in Rose Valley to the east of the field (Fig. 2). The pumping was suspended for one year by the Inyo County, starting in June 2016, due to drawdown of the water table.

The main subject of the present work is the detection and characterization of surface deformation, which is commonly performed in geothermally producing areas (e.g., Kagel, et al., 2007). When such operations take place in tectonically active areas, surface displacements are due to both natural and anthropogenic effects. Monitoring of surface deformation presents possibilities for reservoir management and planning, subsurface fluid flow assessment, impact
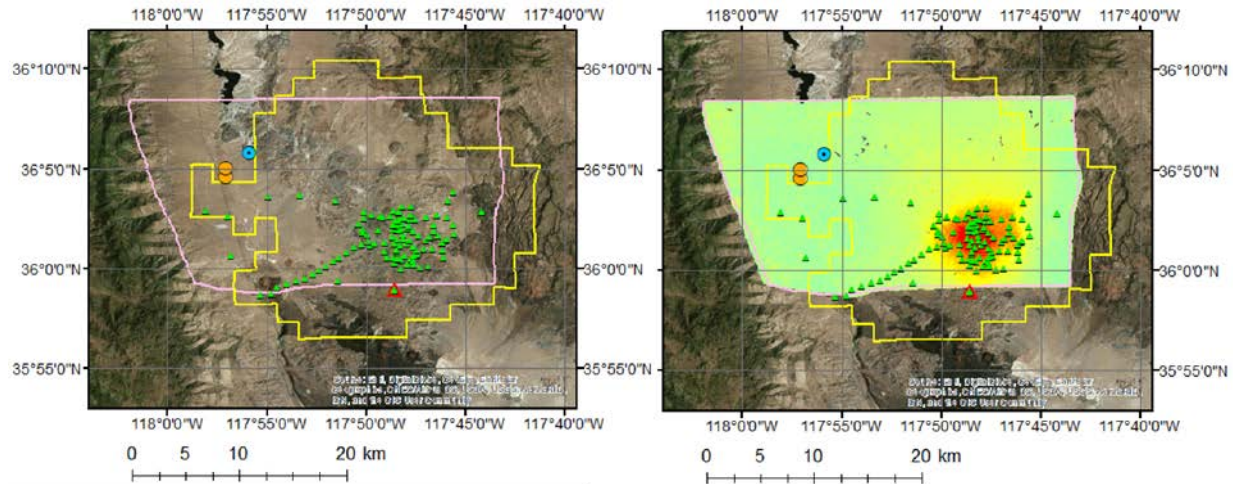
Figure 2. Map of extended study area. Yellow outline – Coso KGRA. Pink outline – InSAR study area. Green triangles – leveling benchmarks. Red triangle – COSO GPS station. Two orange circles – locations of Hay Ranch wells, from which water started being pumped into the CGF in late December, 2009. Blue circle – reference point used in the InSAR analysis. Map on the right – Envisat ascending annual rates of surface deformation, with yellow to red colors indicating subsidence at the CGF.

mitigation, and exploration. Deformation modeling can help assess the proportion of surface change attributable to anthropogenic factors. Understanding of these factors can inform the geothermal operators about the extent and subsurface characteristics of geothermal resources, the effect of particular combinations of production and injection amounts and locations, and possible planning of modifications as needed.

Surface deformation has been traditionally measured by ground-based geodetic data, such as leveling surveys and GPS stations. Measurements of surface deformation from satellites have significantly improved over the last 20 years and are now vastly exceeding the capabilities of ground-based geodetic methods. A special type of radar data, synthetic aperture radar (SAR), are collected and processed with a method known as interferometric SAR (InSAR). Three earlier InSAR studies have analyzed several scenes at Coso from the 1990's (Fialko and Simons, 2000; Wicks, et al., 2001; Vasco, et al., 2002). These early studies suggested downward movements of up to 35 mm/year, and performed deformation modeling suggesting geothermal production zone of depth down to 2.5 km. Here we revisit the subject of deformation detection and modeling, using a total of 203 satellite scenes from two later periods in the 2000's. We are particularly interested in examining changes in time of the subsidence patterns observed at the CGF, as well as in comparing our results with leveling surveys and seismicity.

2. Data

We use SAR data from Envisat (January 2003 – October 2010), Sentinel A (November 2014 – ongoing), and Sentinel B (December 2016 – ongoing). The satellite images from Sentinel A and Sentinel B are processed jointly. The InSAR processing of the data collected over the extended Coso area studied in this project (Fig. 2) provides annual rates of vertical and horizontal surface deformation for two periods, February 2006 – September 2010 (from Envisat), and January 2015

Table 1. Information on the InSAR study area

Parameter	Envisat	Sentinel
Total area size, km^2	449	471
Number of descending/ascending scenes	30 / 45	63 / 65
Minimum repeat interval, days	35	24 by 2017, 12 after
Period of descending/ascending scenes	Jun 2004-Sep 2010/ Feb 2006-Oct 2010	Nov 2014-Apr 2018/ Jan 2015-Apr 2018
Period of vertical and east measurements	Feb 2006-Sep 2010	Jan 2015-Apr 2018
Number of 100-m pixels with measurements of vertical and east movements	35,165	44,546
Average precision vertical rates, mm/year	±0.4	±0.8
Average precision east rates, mm/year	±0.9	±0.9

– April 2018 (from Sentinel). Table 1 shows relevant information about the data sets used and some aspects of the processed results, to be discussed in more detail in Section 3 below. The

terms "descending" and "ascending" refer to the geometry of the satellite trajectories, from north to south and south to north, respectively. Therefore, a total of four sets of satellite data have been processed, two from each satellite.

SqueeSAR processing uses a reference point, making all measurements relative. The reference point in our analysis is shown in Fig. 2, to the northwest from the CGF. Subsequent figures focus on the geothermal field and the reference point remains outside the displayed frames.

Fig. 2 and Figure 3 show 115 leveling benchmarks, for which the GPO has provided data from 13 surveys between 1988 and 2017. A number of benchmarks have been surveyed over shorter periods of time, either starting later, or being used only in the earlier years. Of these surveys, only three took place during the periods covered by the satellite data – two in 2006 and 2009 (Envisat period), and one in the fall of 2017 (Sentinel period). The datum benchmark used in the leveling surveys is B14, 2.6 km southwest from benchmark CE3 that shows the highest level of subsidence among all benchmarks.

The two Hay Ranch wells that started pumping water into the northwestern part of the CGF in late December 2009 (with an interruption between mid-2016 and mid-2017), are also marked in Fig. 2. Figure 4 shows the total monthly production and injection amounts for the geothermal wells at Coso, as reported to the Division of Oil, Gas, and Geothermal Resources (DOGGR, 2018); the addition of water pumped from Hay Ranch is seen clearly in these time series. By March 2018, 21.46x10^9 kg of water has been pumped in the field, which represents close to 20% of the total injection for the same period. The time series of the pumped water was obtained from the Inyo County Water Department (2018).

As part of this project, we have also started incorporating earthquake data for the period March 1996 – April 2015, provided by the U. S. Geological Survey (USGS) (Kaven, et al., 2014). The ultimate goal is to compare comprehensively the earthquake distribution with the satellite deformation data. The earthquakes in the area around Coso are predominantly dextral strike-slip events, consistent with the minimum of 150-170 km of extension that affected the southwestern
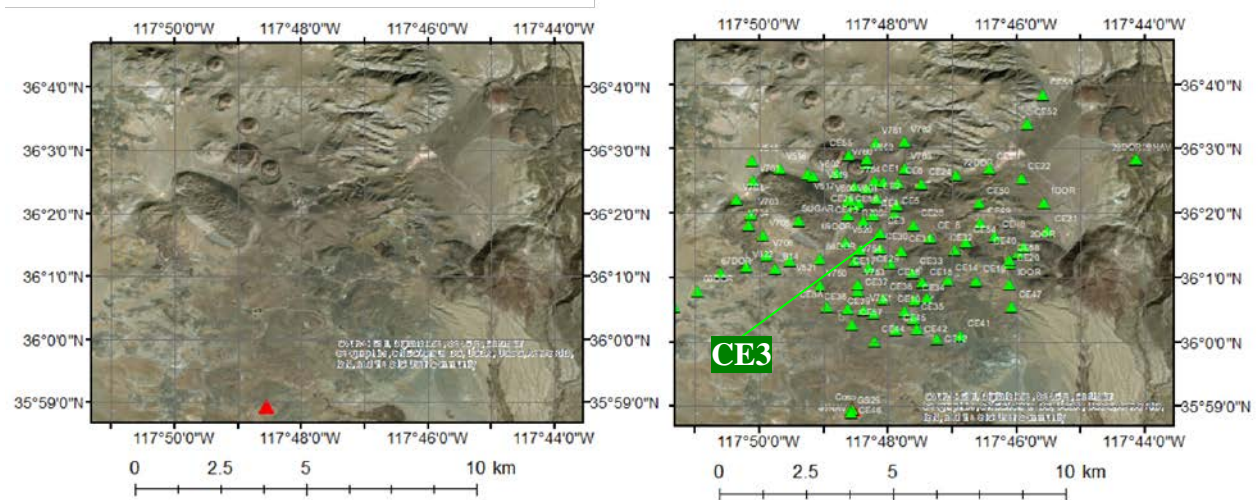
Figure 3. Map of the area focused on the Coso geothermal field. Red triangle – COSO GPS station. Green triangles – leveling benchmarks. Location of maximum subsidence from leveling is at benchmark CE3.
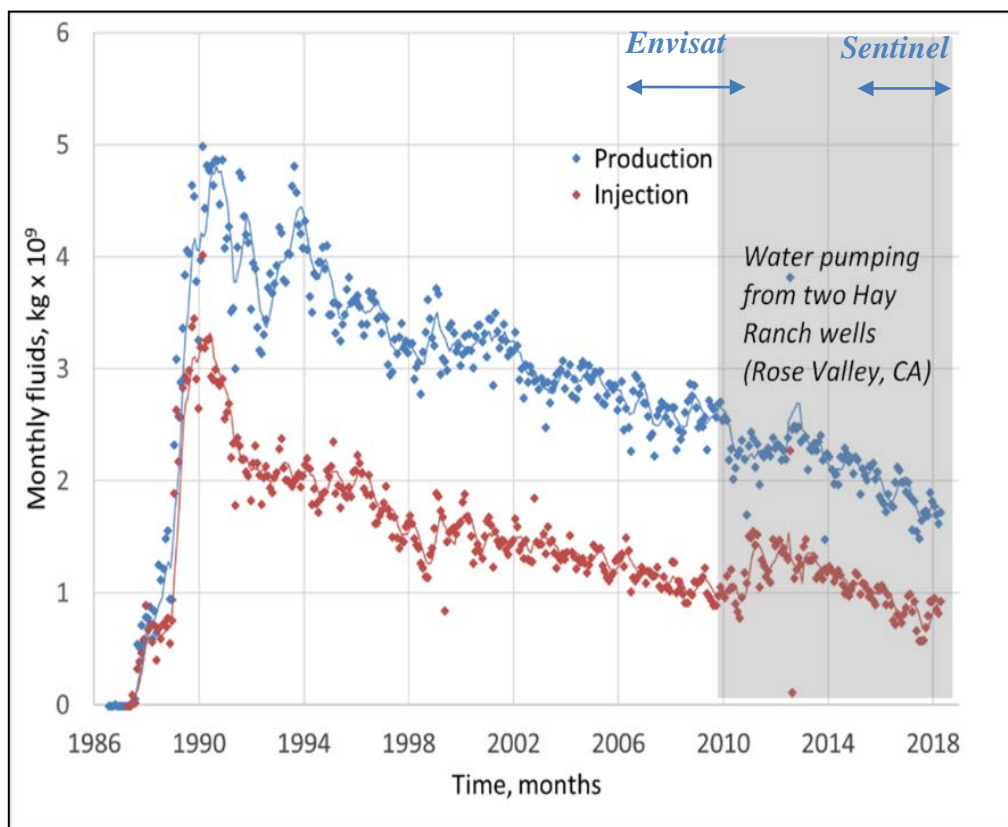

Figure 4. Total monthly amounts of production and injection fluids. The lines show 6-month moving average values. The gray area marks the period of water pumping from Hay Ranch. The Envisat and Sentinel periods are also marked.

Basin and Range region in the late Cenozoic. Recent microseismicity within the field is related to production and injection of fluids and is diagnostic of fracture permeability. Seismic monitoring at Coso began in 1975 with 16 stations operated by the USGS. The U.S. Navy has now a permanent seismometer network operating since the 1980's, which was significantly upgraded in 1992. There have been a number of studies of the seismicity at Coso, both natural and induced. For example, Schoenball, et al. (2015), studied the space-time clustering of microearthquakes and their self-similarity, and Kaven, et al. (2014, 2015) reported on the seismic moment release.

3. Results

3.1 SqueeSAR Technique

The first InSAR technique used to detect surface deformation was differential InSAR (i.e., DInSAR) – see Eneva (2010) for an overview. An innovation, PSInSAR^{TM} (Ferretti, et al., 2007), and its extension, SqueeSAR^{TM} (Ferretti, et al., 2011), developed at TRE Altamira, make it possible to detect deformation in vegetated areas where DInSAR does not work. SqueeSAR makes use of "permanent" and "distributed" scatterers (PS and DS). The PS points can be buildings, well pads, points along roads and canals, fences, lamp posts, transmission towers, rock outcrops, etc. They serve as reflectors of the radar waves that are consistently identified in a sequence of radar scenes, so that time series of surface deformation are derived at each individual PS. The DS represent homogeneous areas emitting signals with smaller signal-to-noise ratios than the PS, but still significantly above the background noise. They include rangelands, pastures, and bare earth that are frequently encountered in relatively arid environments and rural areas. Even in relatively dry areas, where the conventional DInSAR technique works, the newer scatterer-based techniques are still superior with their capability to provide time series at thousands of locations. Throughout this paper, we use the more generic term "InSAR," with which, unless stated otherwise, we mean the SqueeSAR technique.

The deformation is first measured in the line-of-sight (LOS) to the satellite, with negative and positive LOS displacements indicating movements away from and toward the satellite, respectively. Deformation time series are obtained at each PS and DS point and are used to calculate annual deformation rates from the slopes of straight lines fitted to the time series. When these are obtained from both descending and ascending satellite images, it is possible to decompose the two sets of LOS movements into vertical and horizontal components. The satellite orbital geometries of all past and current satellites with SAR instruments on board allow only the determination of the east horizontal component, while the north component generally cannot be recovered (e.g., Wright, et al., 2004; Wicks, et al., 2013). In the Coso area, the sensitivities of Envisat ascending (descending) to the vertical, east horizontal, and north horizontal components are 91% (93%), 41% (38%), and 8% (8%) (i.e., not recoverable), respectively. The sensitivities of Sentinel are 78% (75%), 62% (66%), and 11% (12%), respectively. The SAR instruments on both satellites are right-looking, in direction perpendicular to the satellite trajectory, and downward under a relatively steep look (incident) angle from the vertical to the ground, especially for Envisat. This leads to LOS measurements that are more sensitive to the vertical displacements than to the east horizontal ones, more so for Envisat, so that LOS movements away from or toward the satellite are often indicative of subsidence or uplift, respectively. For this reason, the LOS and vertical deformation maps often display similar spatial patterns, but the numerical values are different. In our previous work we have applied
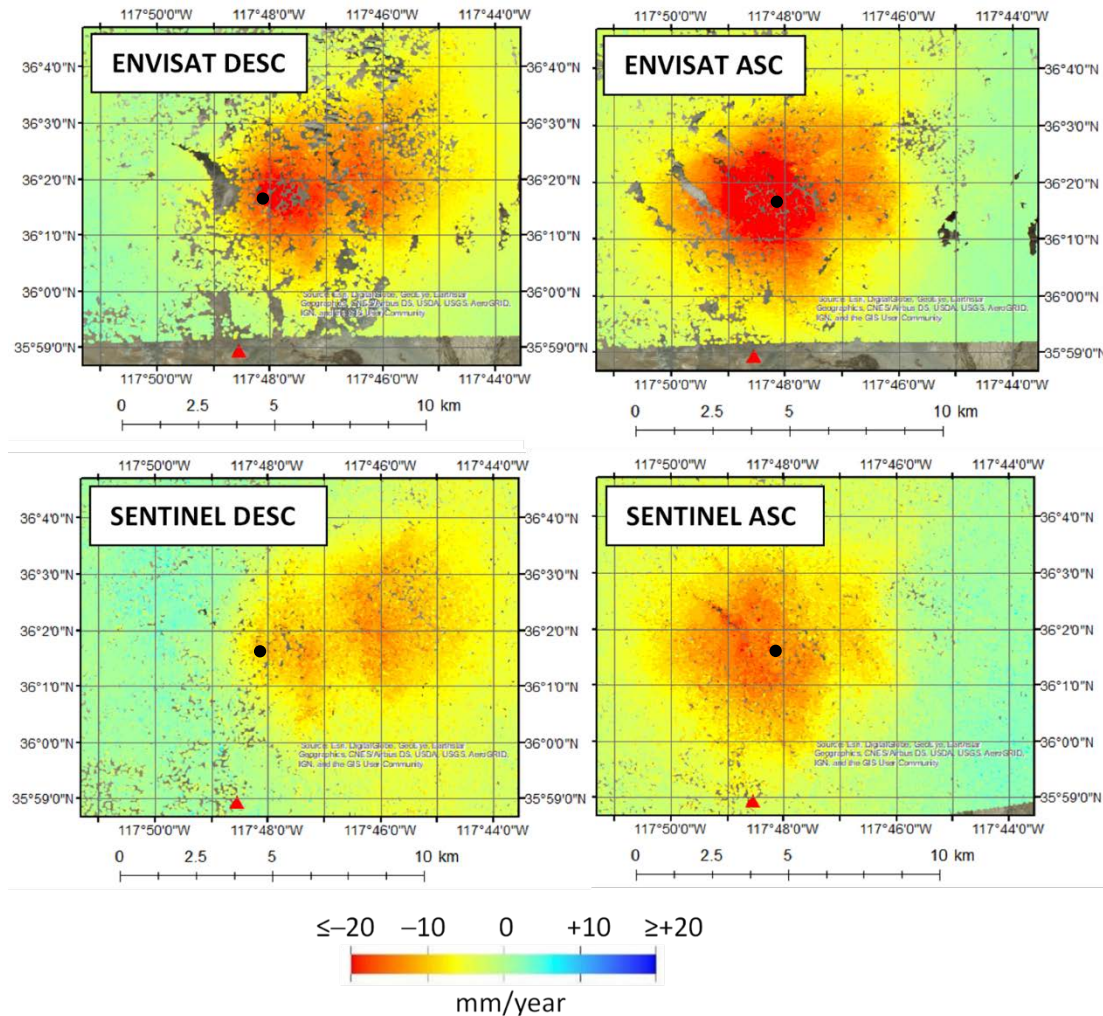
Figure 5. Maps of surface deformation rates derived from the SqueeSAR processing of descending and ascending Envisat and Sentinel satellite radar images. Deformation rates at individual points are color-coded according to color bar on the bottom. Black circle - location of CE3 benchmark. Red triangle – location of COSO GPS station.

PSInSAR and SqueeSAR in geothermal fields of southern California and northern Nevada (Eneva et al., 2009-2014; Ayling et al., 2018). The present work represents an extension of earlier DInSAR studies at Coso, using satellite images from the early 1990's collected by the ERS-1/2 satellites (Fialko and Simons, 2000; Wicks, et al., 2001; Vasco, et al., 2002).

3.2 Surface Deformation from InSAR and Changes in Time

Figure 5 shows maps of the descending and ascending LOS surface deformation rates from Envisat (February 2006 – September 2010) and Sentinel (January 2015 – April 2018). The focus in this figure is on a 93 km^2 area encompassing the CGF. The rates are shown for tens of thousands individual PS/DS points. The number of scatterers commonly identified in dry areas, such as that of the CGF, give the appearance of continuous spatial coverage (except for obvious
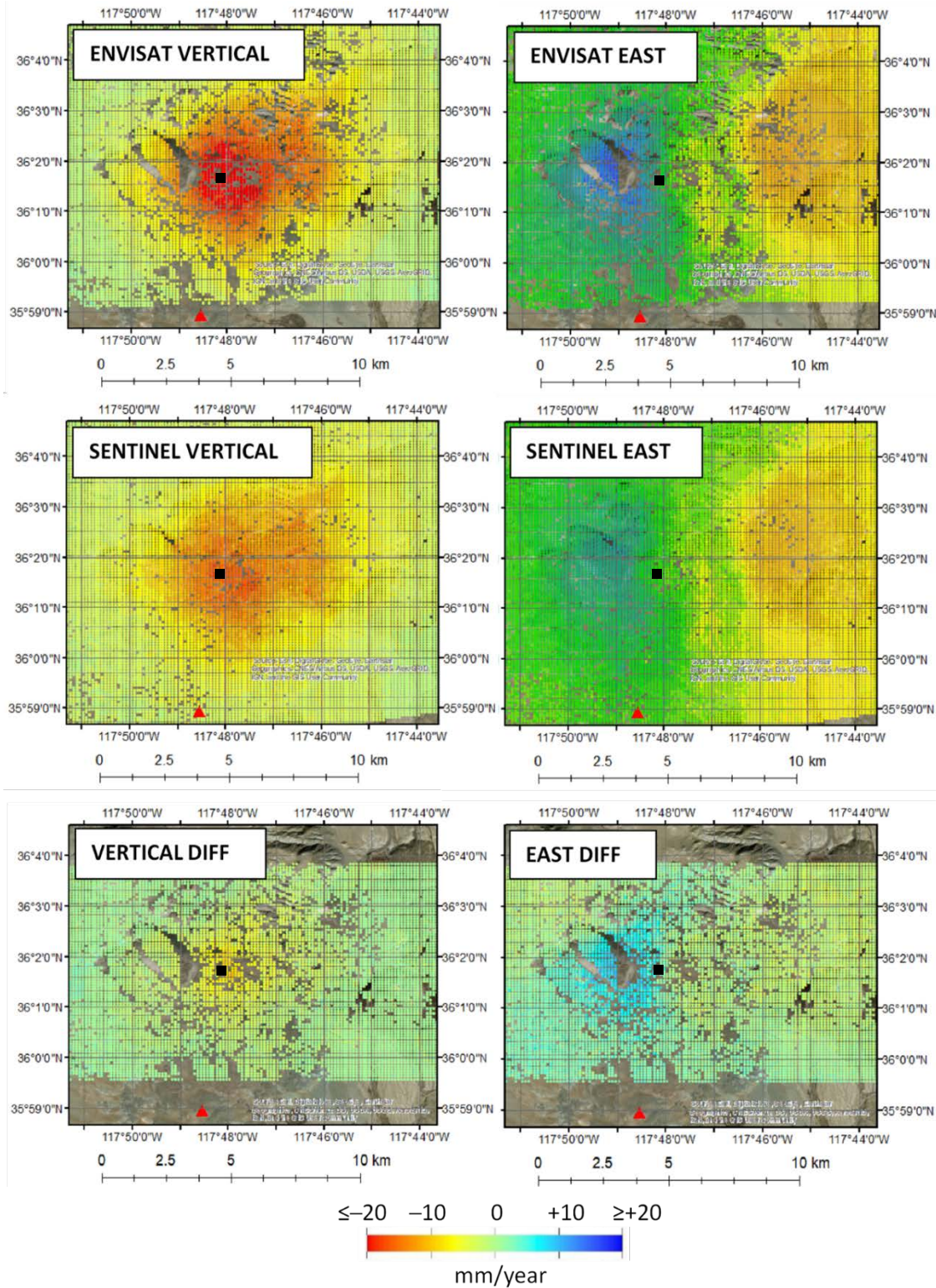
Figure 6. Maps of vertical and east horizontal surface deformation rates in 100-m pixels, as measured from Envisat, Sentinel, and their differences. Vertical rates at individual points are color-coded according to color bar to the left. Black circle – location of benchmark CE3. Red triangle – location of COSO GPS station.

data gaps). Because the color scale is identical for these maps, it is clear that the surface deformation has decreased with time (from Envisat to Sentinel). In Figure 6, the LOS results are further used to calculate the average vertical and east horizontal deformation rates from the individual PS/DS rates within 100-m pixels. This is only possible for pixels with both types of LOS measurements; if one or both are missing, the pixel remains empty. The striped appearance of the maps in Fig. 6 is due to the 100-m grid used for the pixels.

Figs. 5 and 6 show that the Sentinel spatial coverage is significantly better than the Envisat one. Of the 9280 100-m pixels for the area shown in Fig. 6, 83.9% versus 97.5% are with vertical and east values from the Envisat and Sentinel data, respectively (Table 2). In this paper we use negative numbers for subsidence and westward movements, and positive numbers for uplift and eastward movements. The maximum subsidence from Envisat, –27.6 mm/year, is observed 75 m from benchmark CE3, while the maximum subsidence from Sentinel is –19.1 mm/year in the same vicinity. For the east component, the maximum eastward rates are +23.9 mm/year and +15.9 mm/year from Envisat and Sentinel, respectively. The change in the maximum westward rate is significantly smaller, –14.2 mm/year to –11.9 mm/year. The bottom panels of Fig. 6 show difference maps for 82.4% of the 100-m pixels that have both Envisat and Sentinel values.

Table 2. Information on the small area focused on the Coso geothermal field

Parameter	Envisat	Sentinel	Diff
Number/% of 100-m pixels with vertical & east values (of 9,280)	7,790/ 83.9%	9,049/ 97.5%	7,650/ 82.4%
Max/min vertical rates, mm/year	–27.6 (S)/+3.8 (U)	–19.1 (S)/+0.7 (U)	–10.6/+5.4
Max/min east horizontal rates, mm/year	–14.2 (W)/+23.9 (E)	–11.9 (W)/+15.9 (E)	–6.1/+5.4

Table 2 notes: Diff = difference between Envisat and Sentinel measurements, S = subsidence, U = uplift, W = westward horizontal movements, E = eastward horizontal movements.

Surface deformation rates are derived from the slopes of straight lines fitted to the InSAR time series. These can be calculated for individual PS/DS points, individual pixels, or as average values over areas of interest. Figure 7 shows an example of an average time series derived from the Envisat vertical rates at several individual 100-m pixels around the leveling benchmark showing maximum subsidence, CE3.

Figure 8 provides a complementary representation of the trends discussed above. It shows pixel-to-pixel comparison of the vertical and east rates from Envisat and Sentinel. It is evident that while the smaller subsidence rates are not very different between the two satellites, subsidence exceeding ~10 mm/year is notably decreasing during the later time period covered by Sentinel. For the horizontal component, the pixel-to-pixel comparison of westward rates does not indicate a significant difference between the two satellites, but the eastward movement is greatly diminished during the Sentinel period. This analysis can be ultimately done much more comprehensively, by examining average time series at specific locations and deformation rates along profiles associated with geothermal plants, individual wells, faults, structural features, etc.
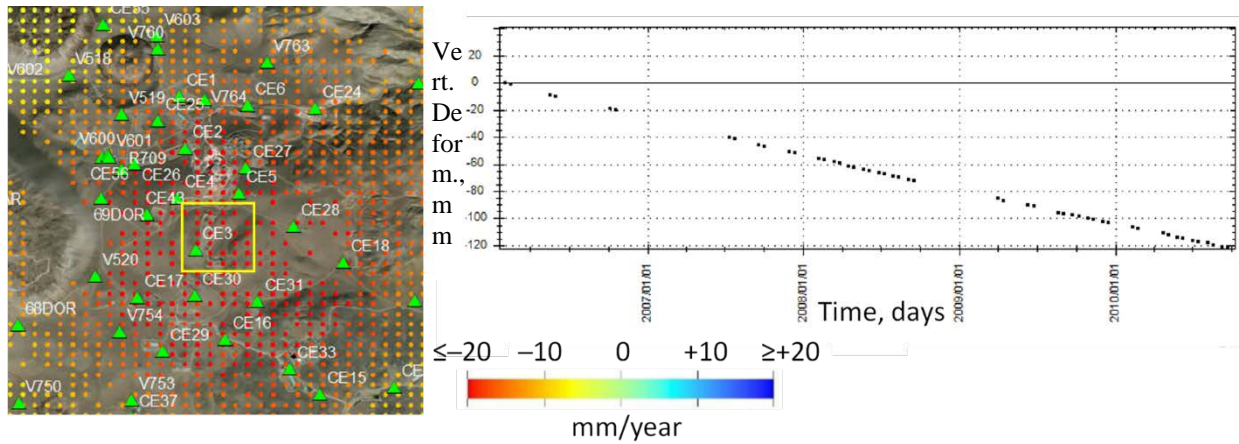
Figure 7. Example of a time series of the average subsidence in a 500 m x 500 m area (yellow outline) including benchmark CE3. Vertical rates at individual points are color-coded according to color bar.
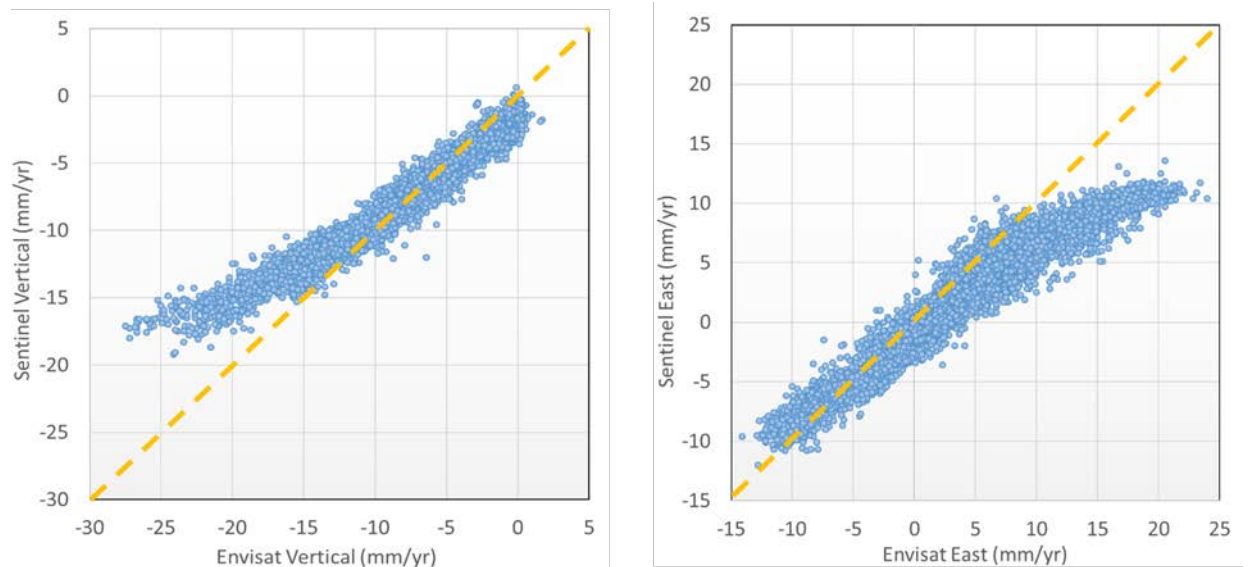

Figure 8. Comparison of annual surface deformation rates from Envisat and Sentinel (i.e., for two different time periods). Yellow dashed lines show where rates would cluster if they were similar during the two periods. Left – comparison of vertical rates. Right – comparison of east horizontal rates.

To our knowledge, there have been three DInSAR studies published earlier using data from ERS-1/2, two satellites preceding Envisat and Sentinel. Vasco, et al. (2002) used seven descending and two ascending images from the five-year period 1992 – 1997 to form five descending pairs and one ascending pair. They reported LOS deformation rates in the –20 to – 30 mm/year range away from the satellite. Because of the steep look angle from the satellite, this strongly suggests subsidence (but is not quite the same). Fialko and Simons (2000) used 8 pairs

from the period 1993-1999 and reported a peak subsidence rate of ~35 mm/year. The same rate was reported by Wicks, et al. (2001), for the period 1992-1997. None of these studies had at their disposal the abundant data available now, and at that time ascending data were scarce, making it unrealistic to perform decompositions into vertical and east components. Also, PS-based techniques were not available at the time, and they would need a significantly larger number of images to work properly. With all these limitations, for direct comparison, we use our maximum away-from-satellite LOS deformation rates (rather than the vertical rates), which are –30.7 mm/year for Envisat and –22.8 mm/year for Sentinel. Compared with the two latter publications using data from the 1990's, it appears then that the subsidence might have been decreasing over the whole 1997-2018 period.

To make a comparison with the leveling data relative to benchmark B14 positioned 2.6 km southwest from CE3, we first look at InSAR measurements around B14, which show similar subsidence rates from Envisat and Sentinel, of –6.7 ± 0.5 mm/year and –5.9 ± 0.9 mm/year, respectively; i.e., change in time is little, if any, compared with other areas of the field. At CE3, where leveling indicates the largest subsidence, the rate (datum B14) from two surveys in 2006 and 2009 (during the Sentinel period) is –21.5 mm/year, and the rate from two surveys in 2013 and 2017 (partially overlapping with the Sentinel period) is –17.0 mm/year. To translate this into the InSAR reference frame, we obtain –28.2 mm/year (= –21.5 – 6.7) for 2006 to 2009 and –22.9 mm/year (= –17.0 – 5.9) for 2013 to 2017. Comparing the first estimate with the maximum subsidence derived from InSAR, –27.6 mm/year, for the Envisat period (2006 – 2010), the agreement is excellent. The estimate from leveling may be slightly higher only because the subsidence was larger at earlier times, and the leveling period considered ends in 2009, one year before the end of the Envisat period (2006 – 2010). The second leveling estimate also agrees well with the maximum InSAR subsidence of –19.1 mm/year for the Sentinel period (2015 – 2018); again, the higher value can be attributed to the earlier survey period (2013 – 2017).

Because the InSAR and leveling values cited above are relative to different reference points, we can get a sense for the absolute movements if the annual rate at the COSO GPS station to the south of the CGF is considered. This station exhibits subsidence at –4.4 ± 0.2 mm/year and a more significant westward movement at –16.4 ± 0.1 mm/year relative to the North American Plate; these measurements are from the Scripps Orbit and Permanent Array Center (SOPAC, 2018). It moves northward as well, at a rate of +3.2 ± 0.1 mm/year, but this is irrelevant in the InSAR framework, because the north component cannot be recovered. For comparison, the InSAR measurements around the COSO GPS for the Sentinel period indicate subsidence of –3.5 ± 0.4 mm/year and eastward movement of +5.8 ± 1.0 mm/year. The station location was not included in the Envisat study area and is 500 m south of its edge. Envisat measurements at the edge indicate subsidence of 3.0 ± 0.9 mm/year and eastward movement of +2.6 ± 1.1 mm/year.

3.3 Earthquake Cross-Sections

Figure 9 displays a map showing that a large portion of the earthquakes cluster around the production area, where the subsidence is also focused. Cross-sections of hypocenters along four profiles are also shown. We use earthquake data from Kaven et al. (2014) for the period March 1996 – early April 2015. The catalog contains more than 80,500 earthquakes with magnitudes M > –1, more than 400 events of M > 3, and more than 100 events of M > 4. Because of improving thresholds of recording with time, 83% of the events in the catalog are from the last 15 years of the catalog. Cross-sections from the Envisat period (February 2006 – September 2010), not

shown in Fig. 9, display similar spatial distributions, but with fewer earthquakes. At present, the catalog includes only a few earthquakes from the first three months of the Sentinel period.
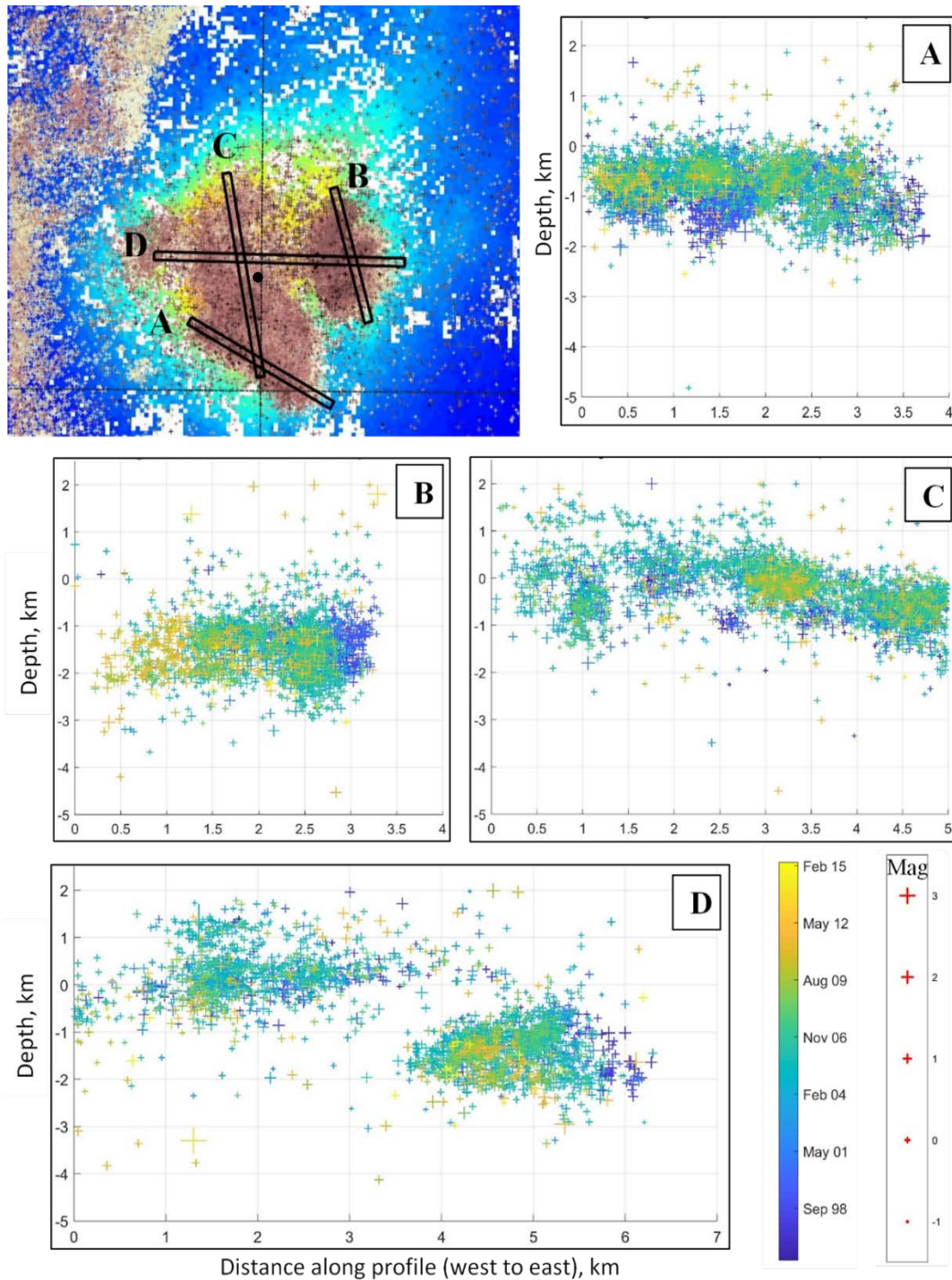

Figure 9. Earthquake cross-sections along four profiles with 200-m width. Map shows epicenters (brown crosses) on top of the vertical surface deformation rates. Black circle marks the location of CE3. The hypocenters in the cross-sections are colored according to time and sized according to magnitude, as indicated by the bars on the bottom right.

3.4 Deformation Modeling

Previous studies (Fialko and Simons, 2000; Vasco, et al., 2002) have relied on elasticity to characterize the distribution volumetric strain rates within the reservoir. Because these studies lacked time-varying estimates of surface motion, they could do very little to characterize the time-varying poroelastic response of the reservoir to injection and production of geothermal fluids. The new data here afford an opportunity, as a first cut, to test analytical solutions to the problem of reservoir depletion in a poroelastic framework (Segall, 1985, 1989).

To justify using a poroelastic model, we compared synthetic position estimates using the formulation given in Segall (1985) to the leveling data (Figure 10). Simulation parameters are taken from reported volumes and general linear poroelastic properties of rock (Wang, 2000). The synthetic data show clear similarities with our data, including axial symmetry and a generally non-linear decrease in subsidence rates over time and radially from the source. Poroelasticity is thus a highly plausible physical explanation for the observed leveling data, implying that the observed subsidence distribution represents the effect of relatively steady net fluid loss at the CGF since the late 1980's.
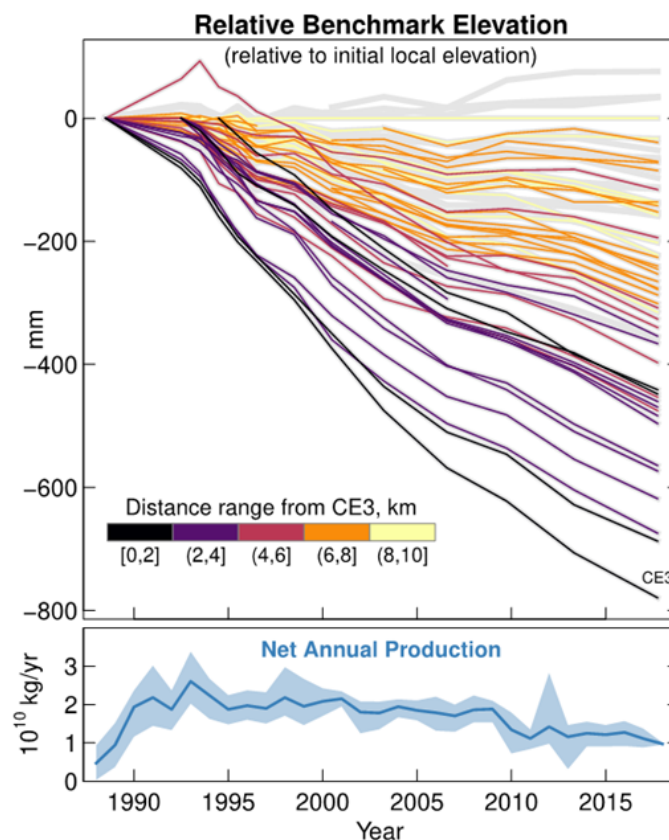

Figure 10. Time series of the relative positions of the leveling benchmarks (top). Benchmarks with fewer than three measurements are not shown. Color indicates radial distance to the fastest-subsiding benchmark, CE3. A time series of the annual net geothermal fluid mass (production minus injection) is shown on the bottom.
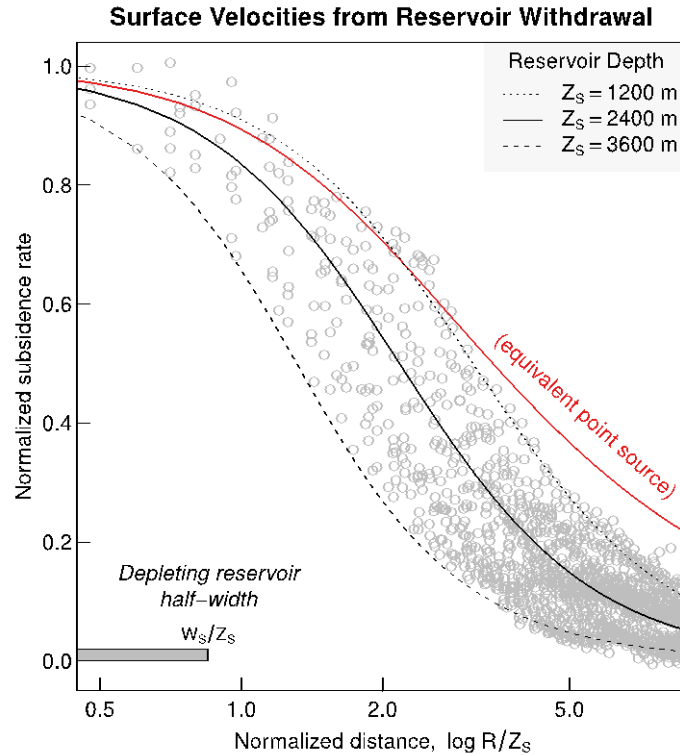
Figure 11. Normalized subsidence rates as a function of normalized distance for a deflating disk-shaped reservoir (Segall, 1989) compared to normalized, spatially averaged subsidence rates from InSAR (circles; see Fig. 6); the origin is at benchmark CE3. The spatial profile of subsidence is best matched with a reservoir with finite dimensions, as opposed to an equivalent point-source model (i.e., Segall, 1985). The best fitting depth is $Z_S \approx 2.4$ km with a half-width of 0.8 times the source depth, and a thickness of a few hundred meters.

Further insight into the connection between net production and observed surface rates is gained from incorporating the InSAR vertical rates from the Envisat satellite (shown in the top left corner of Fig. 6), which allows us to independently constrain the source depth likelihood, and to test whether there is an appreciable effect of reservoir structure on the observed rates. In particular, we modify the approach of Barbour, et al. (2016), which treats the surface velocities as the manifestation of a point source of volumetric strain at depth, to include finite reservoir dimensions (i.e., Segall, 1989); then, systematic non-linear inversions are used to identify the regions of maximum likelihood. Based on previous studies, we expect this depth to be from about 1.5 to 2.5 km below the surface, and a systematic fitting procedure shows a probable depth range between 1.2 and 3.6 km, with the most probable depth at 2.4 km (Figure 11). In comparison with the equivalent point-source solution (i.e., Segall, 1985), this finite-source solution shows a significantly improved fit to the data.

As we have shown, the spatial and temporal characteristics of the leveling and InSAR data closely match the expected movements from a simplified model of a contractional volumetric strain source embedded in a uniform, poroelastic half space. Using the maximum likelihood depth (2.4 km), we apply Simulated Annealing (Belisle, 1992) to solve for optimal values of
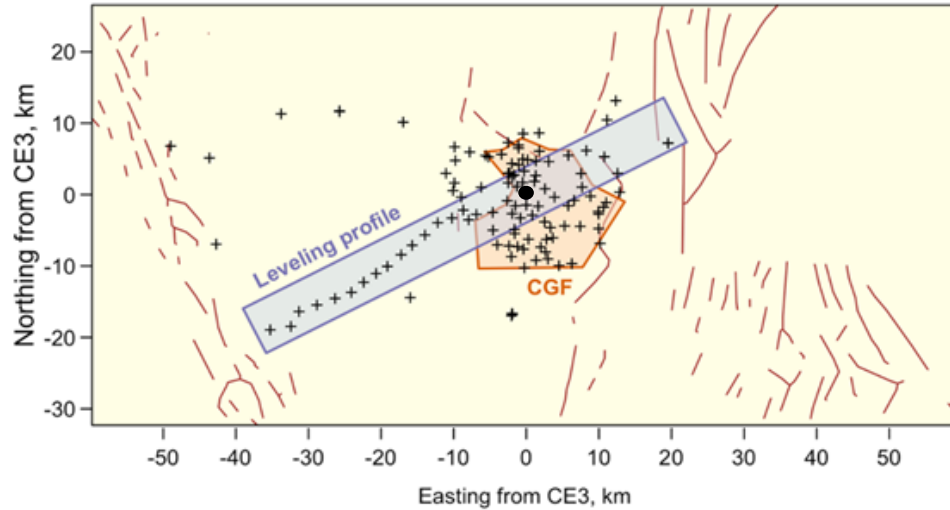
Figure 12. Map showing the leveling benchmarks (crosses) and a profile of leveling data used in subsequent figures (diagonal strip). Black circle - location of benchmark CE3.

hydraulic diffusivity and volumetric loss rates at sources distributed across the reservoir, along a profile that passes through benchmark CE3 (Figure 12).

In general, the optimal results are in good agreement with data along the leveling profile (Figure 13), however there are locations where additional sources might be present, as the residual positions show. This is punctuated by the observation that the InSAR data are best represented by a contracting reservoir with finite dimensions rather than a layer with infinitesimal thickness (Figure 11).
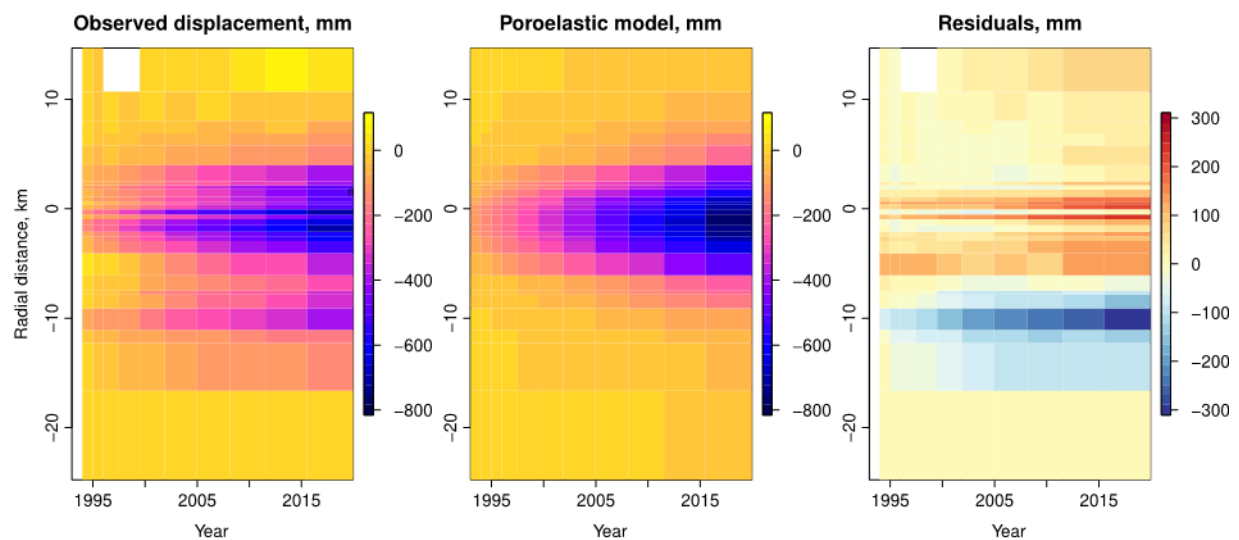

Figure 13. Observed relative displacements along the leveling profile as a function of time, and the time series predicted by the optimal poroelastic model. The image on the right shows the residual displacements (observed minus modeled), highlighting areas that are possibly influenced by additional sources of deformation.

The optimal diffusivity estimate based on ground deformation is ~0.01 m^2/s, which is consistent with the lower range of estimates from seismicity migration patterns (Chen, et al., 2012). It is important to note, however, that the leveling surveys were not performed uniformly in space and time, so the first data from some benchmarks were not collected until well after benchmark CE3 was surveyed. Consequently, we expect that this non-uniform data coverage has introduced a parameter bias, because the profile of relative positions used in the optimization is inaccurate; this is a problem which is especially acute at short radial distances (assuming the poroelastic model is valid). One limitation of our modeling is that we do not account for spatially variable rates of geothermal fluid injection and production, as suggested by dense geodetic data, although this is unavoidable because those data are presently unavailable. Another limitation is that we have we included information on well completion (e.g., open hole intervals) which may alter the spatial distribution of modeled values.

The optimal set of properties for the hypothetical depleting reservoir and the hydraulic diffusivity of the medium are in close agreement with previous work characterizing the geothermal system and local-to-regional scale patterns in seismicity. However, without new sources of data, such as time series of production and injection fluids for individual wells, the preexisting feedback between permeability and moment release – seismic or otherwise – may be largely inseparable from the changes induced by anthropogenic production of the resource.

4. Conclusions

We have successfully applied radar interferometry (InSAR) to measure rates of vertical and horizontal surface deformation at the Coso Geothermal Field (CGF) in two different time periods, February 2006 – September 2010 and January 2015 – April 2018, using data from the Envisat and Sentinel satellites, respectively. We observe a significant subsidence in the field, decreasing with time, with maximum rates of –27.6 mm/year and –19.1 mm/year in the earlier and later periods, respectively. These observations appear to also indicate a decreasing subsidence rate compared with more limited InSAR studies in the 1990's. Significant eastward movements are also observed, with rates decreasing from +23.9 mm/year to +15.9 mm/year, while westward movements are smaller and change less with time (–14.2 mm/year to –11.9 mm/year). These InSAR observations agree with leveling surveys conducted in the area. Both types of geodetic measurements support a poroelastic model of the geothermal resource, with most probable depth of 2.4 km, in agreement with previous studies. Earthquakes cluster prominently in the area of subsidence, and their cross-sections along representative profiles suggest show clusters at different depths.

Future analysis will include joint earthquake and deformation maps and cross-sections, average deformation time series at specific locations, and deformation rates along profiles. Areas and profiles of particular interest could be associated with geothermal plants, individual wells, faults, structural features, etc. Future plans include processing of additional Sentinel scenes from the period May 2018 – September 2019. We will also compare the deformation observations with other geophysical data, such as LiDAR (Blake, et al., 2018), gravity, seismic velocities (Vp and Vs), and magnetotelluric data.

Our work demonstrates that InSAR provides high-accuracy spaceborne geodetic measurements of unprecedented dense spatial and temporal coverage, which have great potential to aid geothermal operators in reservoir management. However, at time of writing, the data analysis is

limited by the lack of time series of production and injection for the individual wells. The only well data available at this time are the wellbore locations and the total monthly amounts of production and injection, which are insufficient to address implications for the field operations. Should the individual well histories become available in the future, we will compare them quantitatively to the InSAR and leveling surface deformation measurements, as well as to the induced seismicity, in an effort to derive useful strategies for data-driven reservoir management.

5. Acknowledgments

REFERENCES

Ayling, B. and the Fallon FORGE team (36 co-authors). "Phase 2 Update for the Fallon FORGE Site, Nevada, USA." *Proceedings: 43rd Workshop on Geothermal Reservoir Engineering*, Stanford University, Stanford, CA, (2018), SGP-TR-213.

Barbour, A.J., Evans, E.L., Hickman, S.H., and M. Eneva. "Subsidence Rates at the Southern Salton Sea Consistent with Reservoir Depletion." *J. Geophys. Res.*, 121(7), (2016), 5308-5327, doi: 10.1002/2016JB012903.

Belisle, C.J.P. "Convergence Theorems for a Class of Simulated Annealing Algorithms on Rd." *J. Applied Probability*, 29(4), (1992), 885-895, doi: 10.2307/3214721.

Blake, K., Sabin, A., Lazaro, M., Tiedeman, A., Meade, D., and Huang, W.-C. "LiDAR Analysis over the Coso Volcanic Field, CA." *Geothermal Resources Council Transactions*, 42 (2018).

Chen, X., Shearer, P.M., and Abercrombie, R.E. "Spatial Migration of Earthquakes Within Seismic Clusters in Southern California: Evidence for Fluid Diffusion." *J. Geophys. Res.*, 117(B4), (2012), doi: 10.1029/2011JB008973.

Division of Oil, Gas, and Geothermal Resources - http://www.conservation.ca.gov/dog/; DOGGR website accessed on June 5, 2018.

Eneva, M., Adams, D., Falorni, G., Novali, F., and Hsiao, V. "Surface Deformation at the Salton Sea Geothermal Field from High-Precision Radar Interferometry." *Geothermal Resources Council Transactions*, 38, (2014), 991-999.

Eneva, M., Adams, D., Falorni, G., and Morgan, J. "Application of Radar Interferometry to Detect Subsidence and Uplift at the Heber Geothermal Field, Southern California," *Geothermal Resources Council Transactions*, 37, (2013), 491-499.

Eneva, M., Adams, D., Falorni, G., and Morgan, J. "Applications of Radar Interferometry to Detect Surface Deformation in Geothermal Areas of Imperial Valley in Southern California." *Proceedings: 38th Workshop on Geothermal Reservoir Engineering*, Stanford University, Stanford, CA (2013), SGP-TR-198.

Eneva, M., Adams, D., Falorni, G., and Morgan, J. "Surface Deformation in Imperial Valley, CA, from Satellite Radar Interferometry." *Geothermal Resources Council Transactions*,36, (2012), 1339-1344.

Eneva, M., Falorni, G., Teplow, W., Morgan, J., Rhodes,G., and Adams, D. "Surface Deformation at the San Emidio Geothermal Field, Nevada, from Satellite Radar Interferometry." *Geothermal Resources Council Transactions*, 35, (2011), 1647-1653.

Eneva, M. "Detection of Surface Deformation at Mining and Geothermal Sites Using Satellite Radar Interferometry (InSAR)." *Proceedings: 44th U.S. Rock Mechanics Symposium and 5th U.S. – Canada Rock Mechanics Symposium*, Salt Lake City, UT (2010).

Eneva, M., Falorni, G., Adams, D., Allievi, J., and Novali, F. "Application of Satellite Interferometry to the Detection of Surface Deformation in the Salton Sea Geothermal Field, California.", *Geothermal Resources Council Transactions*, 33, (2009), 315-319.

Ferretti, A., Fumagalli, A., Novali, F., Prati, C., Rocca, F., and Rucci, A., 2011, A New Algorithm for Processing Interferometric Data-Stacks: SqueeSAR." *IEEE Trans. Geosc. Remote Sensing*, 49(9), (2011), 3460-3470.

Ferretti, A., Savio, G., Barzaghi, R., Borghi, A., Musazzi, S., Novali, F., Prati, C. and Rocca, F. 2007, "Submillimeter Accuracy of InSAR Time Series: Experimental Validation." *IEEE Trans. Geosc. Remote Sensing*, 45, (2007) 1142-1153.

Fialko, Y., and Simons, M. "Deformation and Seismicity in the Coso Geothermal Area, Inyo County, California: Observations and Modeling Using Satellite Radar Interferometry." *J. Geophys. Res.*, 105, (2000), 21781-21793.

Inyo County Water Department - http://www.inyowater.org/projects/groundwater/coso-hay-ranch-project/; Coso-Hay Ranch Project website accessed on June 1, 2018.

Kagel, A., Bates, B., and Gawel, K. "A Guide to Geothermal Energy and the Environment." Geothermal Energy Association (2007), 75 pp.

Kaven, J.O., Hickman, S.H., and Davatzes, N.C. "Seismicity and Deformation in the Coso Geothermal Field from 2000 to 2012." *Geophys. Res. Abstracts*, 17, (2015), EGU2015-14466.

Kaven, J.O., Hickman, S.H., and Davatzes, N.C. "Micro-Seismicity and Seismic Moment Release within the Coso Geothermal Field, California." *Proceedings: 39th Workshop on Geothermal Reservoir Engineering*, Stanford, CA (2014), SGP-TR-202.

Kaven, J. O., Hickman, S.H., and Davatzes, N.C. "Mapping of Fluid Compartments with Microseismicity and Seismic Velocities within the Coso Geothermal Field, California." *Proceedings: 37th Workshop on Geothermal Reservoir Engineering*, Stanford University, Stanford University, Stanford University, CA, (2012) SGP-TR-194.

Kaven, J.O., Hickman, S.H., and Davatzes, N.C. "Micro Seismicity, Fault Structure and Hydraulic Compartmentalization within the Coso Geothermal Field, California." *Proceedings: 36th Workshop on Geothermal Reservoir Engineering*, Stanford University, Stanford, CA, (2011), SGP-TR-191.

McClusky, S.C., Bjomstad, S.C., Hager, B.H., King, R.W., Meade, B.J., Miller, M.M., Monastero, F.C., and Souter, B.J. "Present Day Kinematics of the Eastern California Shear

Zone from a Geodetically Constrained Block Model." *Geophys. Res. Lett.*, 28(17), (2001), 3369-3372.

Monastero, F.C., Katzenstein, A.M., Miller, J.S., Unruh, J.R., and Richards-Dinger, K. "The Coso Geothermal Field: A Nascent Metamorphic Core Complex." *Geol. Soc. Amer. Bull.*, 117(11-12), (2005), 1534-1553.

Monastero, F.C., "An Overview of Industry-Military Cooperation in the Development of Power Operations at the Coso Geothermal Field in Southern California." *Geothermal Research Council Bulletin*, 31(5), (2002), 188-195.

Newman, G.A., Gasperikova, E., Hoversten, G.M., and Wannamaker, P.E. "Three-Dimensional Magnetotelluric Characterization of the Coso Geothermal Field." *Geothermics*, 37, (2008) 369–399.

Schoenball, M., Davatzes, N.C., and Glen, J.M.G. "Differentiating Induced and Natural Seismicity Using Space-Time-Magnitude Statistics Applied to the Coso Geothermal Field." *Geophys. Res. Lett.*, 42, (2015), 6221-6228, doi:10.1002/2015GL064772.

Scripps Orbit and Permanent Array Center (SOPAC) – http://sopac.ucsd.edu/); SOPAC website accessed on May 20, 2018.

Segall, P. "Earthquakes Triggered by Fluid Extraction." *Geology*, 17(10), (1989), 942–946, doi: 10.1130/0091-7613.

Segall, P. "Stress and Subsidence Resulting from Subsurface Fluid Withdrawal in the Epicentral Region of the 1983 Coalinga Earthquake." *J. Geophys. Res.*, 90(B8), (1985), 6801–6816, doi: 10.1029/JB090iB08p06801.

Seher, T., Zhang, H., Fehler, M., Yu, H., Soukhovitskaya, V., Commer, M., and Newman, G. "Temporal Velocity Variation Beneath the Coso Geothermal Field Observed Using Seismic Double Difference Tomography of Compressional and Shear Wave Arrival Times." *Geothermal Resources Council Transactions*, 90, (2011), 1743-1747.

U.S. Geological Survey. "Assessment of Moderate- and High-Temperature Geothermal Resources of the United States." U.S. Geological Survey Fact Sheet 2008-3082 (2008).

Vasco, D.W., Wicks, C., Karasaki, K., and Marques, O. "Geodetic Imaging: Reservoir Monitoring Using Satellite Interferometry." *Geophys. J. International*, 149, (2002), 555-571.

Wang, H.F. "Theory of Linear Poroelasticity with Applications to Geomechanics and Hydrogeology." Princeton Univ. Press, Princeton, N. J. (2000), 304 pp.

Wicks, C., Tatcher, W., Monastero, F., and Hasting, M. "Steady-State Deformation of the Coso Range, East Central California, Inferred from Satellite Radar Interferometry." *J. Geophys. Res.*, 106, (2001), 13769-13780.

Wicks, C., Weaver, C., Bodin, P., and Sherrod, B. "InSAR Evidence for an Active Shallow Thrust Fault Beneath the City of Spokane, Washington, USA." *J. Geophys. Res.*, 118, (2013), doi:10.1002/jgrb.50118.

Wright, T.J., Parsons, B.E., and Lu, Z. "Toward Mapping Surface Deformation in Three Dimensions Using InSAR." *Geophys. Res. Lett.*, 31, (2004), L01607, doi:10.1029/2003GL018827.